Leakage Vortex Progression through a Guide Vane's Clearance Gap and the Resulting Pressure Fluctuation in a Francis Turbine

Nirmal Acharya [1,*], Saroj Gautam [2], Sailesh Chitrakar [2], Chirag Trivedi [1] and Ole Gunnar Dahlhaug [1]

1 Waterpower Laboratory, Department of Energy & Process Engineering, Norwegian University of Science and Technology, NO-7491 Trondheim, Norway; chirag.trivedi@ntnu.no (C.T.); ole.g.dahlhaug@ntnu.no (O.G.D.)
2 Turbine Testing Lab, Kathmandu University, Dhulikhel 45210, Nepal; saroj.gautam@ku.edu.np (S.G.); sailesh@ku.edu.np (S.C.)
* Correspondence: nirmal.acharya@ntnu.no

Abstract: A clearance gap (CG) between guide vanes (GVs) and facing plates exists at both ends of a Francis turbine and allows the opening angle to be adjusted for varying operating conditions. Leakage flow is induced through this gap due to the pressure difference between the two sides of the guide vanes. While some research works have used qualitative approaches to visualize and predict the strength of a leakage vortex (LV), this paper presents a method for quantifying vortices along a trajectory. In this paper, a prototype high-head Francis runner with specific speed of 85.4 is considered as a reference case. A systematic investigation across both space and time is carried out, i.e., analysis of the spatial temporal progression of LV for three operating conditions. While travelling from the CG to runner leading edge, LV evolution and trajectory data are observed and the values of vorticity and turbulent kinetic energy are calculated for the LV trajectory. Frequency spectrum analyses of pressure oscillations in the vaneless space, runner blade, and draft tube are also performed to observe the peak pressure pulsation and its harmonics. Unsteady fluctuations of the runner output torque are finally studied to identify the patterns and magnitudes of torque oscillations.

Keywords: clearance gap; leakage vortex; rotor stator interaction; pressure pulsation

1. Introduction

Francis turbines are the most prevalent reaction turbines, which are normally adopted for medium-head and medium-flow conditions. In these turbines, the flow rate is regulated with guide vanes (GVs) that exist upstream of a runner. Water leaving from the guide vanes enters the runner blades with the desired angle at a high velocity which is consequently converted into rotary motion. In addition, GVs are incorporated with a small clearance gap (CG) at both ends so that they can pitch around their axis, which enables the adjustment of the opening angle based on various operating conditions. Several studies [1–5] have suggested that the sizes of CGs increase with head cover deflection due to water pressure, which results in the disturbance of the runner inlet flow conditions and a loss in overall efficiency. Brekke [1] studied the influence of varying CG and GV sizes on flow behavior and turbine efficiency, observing that the size of the CG has a high influence on the overall turbine efficiency. Thapa [2] developed an experimental setup with a GV cascade representing the flow inside the distributor of a Francis turbine. Pressure and velocity data obtained from his experiments showed that all CG sizes greater than 1 mm induced a turbulent cross-flow jet which mixes with the main flow and disrupts the runner inlet flow conditions. A critical size for maximum leakage flow effects was identified to be 2 mm from his experiments. Chitrakar [3] investigated flow phenomena around GV parameters computationally and compared and validated their results with the experimental results from Thapa [2]. The results showed that flow on the suction side is significantly affected by pressure-to-suction side flow through the gap and that the reduction of the pressure gradient reduces leakage through GVs. Koirala [4] performed a study on GVs at the

Kaligandaki Hydroelectric Power Station, Nepal, with a capacity of 144 W. One of his major observation was that the CG at the trailing edge was larger than leading edge, which was due to the increasing cross flow velocity with a decreasing pressure for a decreasing diameter of the runner. Koirala [5] also studied the effects of the CG on turbine performance. Higher flow-affected regions were observed with a larger gap, which might be due to the substantial pressure variation across vanes. Moreover, the leakage flow rate has been found to increase with an increase in the CG, which ultimately causes pressure drops and efficiency loss in a turbine. Liu [6] investigated a leakage vortex in a mixed flow pump as a turbine (PAT) in the pump mode numerically, which was validated with experimental measurements. He concluded that, although the gap in the study was narrow, it could induce severe leakage vortex and flow separation effects which could remarkably deteriorate the subsequent flow state in the pump and turbine. As GVs have adjacent pressure and suction sides, flow passes through the gaps from the high-pressure side to the low-pressure side or suction side. The fluid flow behavior from a GV is difficult to predict because of the wakes passing through the trailing edge combined with the cross-leakage flow through the CG [1]. This leakage flow is intermixed with the primary flow in the suction side of the GV, thus disturbing the overall flow characteristics.

Over the last few years, both numerical and experimental works have been carried out for the investigation of leakage flow through CGs in Francis turbines. A numerical investigation of the leakage flow in a three-GV cascade rig conducted by Chitrakar et al. showed that leakage flow depends on GV loading and that an asymmetrically profiled GV can improve turbine performance in terms of erosion, efficiency, and pressure pulsations of the runner [7,8]. Chitrakar [7] investigated the performance of a Francis turbine, including erosion-induced CGs on GVs. With a case study of sediment-prone hydropower in Nepal, he concluded that vortices containing sediment erode the inlet of the runner blade towards the hub and shroud. Moreover, asymmetrical GV profiles have been found to have a minimal influence on pressure pulsations at the runner inlet. Chitrakar [8] investigated flow through a CG with cambered hydrofoil shapes by using a particle image velocimetry (PIV) technique. He has inferred that the pressure distribution around the hydrofoil affects the velocity field, leakage flow, and characteristics of the vortex filament developed inside the cascade. Gautam et al. [9] studied leakage flow using an alternative CG method for both asymmetrical and symmetrical GV profiles. The results show that vortices leaving the GV with a NACA 4412 profile travel towards GV surface, whereas in the case of NACA 0012, it strikes the runner inlet. Moreover, FFT analysis depicts that the frequency spectrum at the same operating condition shows lower amplitude regarding pressure pulsation in the case of an asymmetrical GV profile when compared to a symmetrical one for all CG sizes.

During operation, a Francis turbine is subjected to pressure fluctuations that originate from the interactions between rotating and stationary parts of the machine, which is defined as rotor–stator interaction (RSI). RSI describes the unsteady interaction between the rotating flow caused by runner blades (the rotating part) and the flow disturbances caused by the guide vane blades (the stationary parts). This interaction induces pressure waves that propagate through the overall hydraulic machine and hence should be considered; however, the phenomenon and characteristics of pressure fluctuation become more complex and unpredictable when a CG exists [10]. Figure 1a shows an illustration of a pressure pulse occurring as a runner blade passes through a guide vane cascade. The wake originating from the guide vanes enters the runner blade as depicted in Figure 1b [11]. It is well documented in various studies that flow instabilities, such as pressure fluctuation, vortex formation, cavitation, etc., deteriorate the hydraulic turbine efficiency and operating lifetime. Vortex evolution and propagation is a complicated phenomenon and there are several examples of vortex-induced instabilities in hydropower turbines [12]. The unsteady phenomenon in turbomachines can be classified into periodic and non-periodic types [13]. RSIs are associated with the periodic class, whereas vortex rope formation and cavitation, observed at the exit of the runner and in the cone of draft tube, which rely on the operating points, are associated with the non-periodic class.
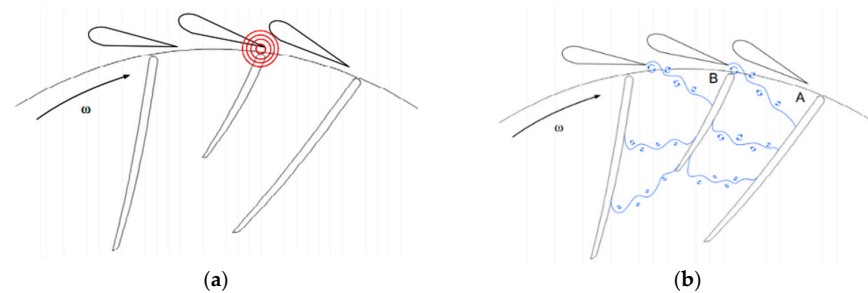
Figure 1. (**a**) Occurrence of a pressure pulse as a runner blade passes through a guide vane cascade; (**b**) GV wake progressing towards the runner. Adapted with permission from Einar Kobro (2010) [11].

Vortex identification can lead to an increased understanding of complex flow phenomena. In complex flow scenarios, as in Francis turbines, there are several interacting vortices which may be bent or twisted, thus resulting in rotation in several different planes for each single vortex. Several systematic procedures for the identification of vortices have been developed and proposed [12–16]. Zhang [12] has performed a review of methods for vortex identification in hydraulic turbines. He has also discussed and summarized experimental techniques for vortex observation. Similarly, Qian [13] has experimentally investigated unsteady flows at the stator level in a Francis turbine model in his doctoral thesis. Chakraborty [14] proposed a local vortex identification criterion and requirements with the introduction of spiraling compactness for material orbits in vortices. Elsas [15] introduced an alternative vortex identification method which he termed as the "*vorticity curvature criterion*", which is fundamentally based on the local properties of the vortex field. He has carried out a realistic comparative study for vortex identification for the direct numerical simulation of a turbulent channel flow. Likewise, ANSYS® has devised several methods to detect vortices as spatial regions with a specified set of equations [16]. The most popularly used criteria include the Q criterion [17], λ2 criterion, [18], Δ criterion [19], and swirling strength criterion (λci) [20]. The Q criterion is relevant for identification of a vortex in incompressible fluid, especially in large scale vortices in turbulent flow. The details of the Q criterion, which is the method of vortex identification in this paper, are discussed in the results section. The λ2 criterion corresponds to the pressure minimum in a plane when the contributions of unsteady irrotational straining and viscous terms in Navier–Stokes equations are discarded. The Δ criterion defines vortices in regions with a complex velocity gradient. A higher value of Δ denotes stronger spiraling within a vortex region. The λci criterion identifies a vortex structure based on the imaginary eigenvalues of the velocity gradient with the quantification of the swirling strength in the vortex. The spatiotemporal evolution of a leakage vortex (LV) in a Francis turbine is still unpredictable and the relationship between flow instability and LV progression has not been revealed completely. Hence, this work is intended to understand the spatiotemporal evolution of LVs and related steady and unsteady flow phenomena in a reference case of a Francis turbine. Moreover, the frequency spectra of pressure signals at various locations inside a turbine are analyzed to understand the RSI and vortex rope phenomena.

2. Methodology

This study uses a prototype turbine with nominal head size of 207 m, rated discharge of 4.33 m^3/s, and rated speed of 750 rpm from the Bhilangana-III Hydroelectric Power Plant, Uttarakhand, India, which is mentioned as the reference turbine onwards. Figure 2 shows the methodology adopted for this research work.

Numerical studies were performed using ANSYS® CFD^{TM} by solving steady-state Reynolds-averaged Navier–Stokes equations. The calculations were conducted at 77%, 100%, and 130% loads and the respective flow rate values were 3.36, 4.34, and 5.64 m^3/s [21]. A 100% load corresponds to the best efficiency point (BEP), whereas the 77% and 130% loads correspond to a partial load (PL) and full load (FL), respectively. Figure 3 shows a numerical model of the reference turbine, which has a runner rotating at 750 rpm and four

stationary domains. The GVs of this powerplant were numerically studied by Acharya et al. earlier with a different runner [22]. Shaft allowance was also included in the GVs for this study to make the numerical case as close as the prototype [22,23]. The full model of the turbine consists of 13 runner blades and 16 GVs, as shown in Figure 2. The draft tube mesh is not shown in the figure. Spiral casing and stay vanes were excluded in the domain during simulation.
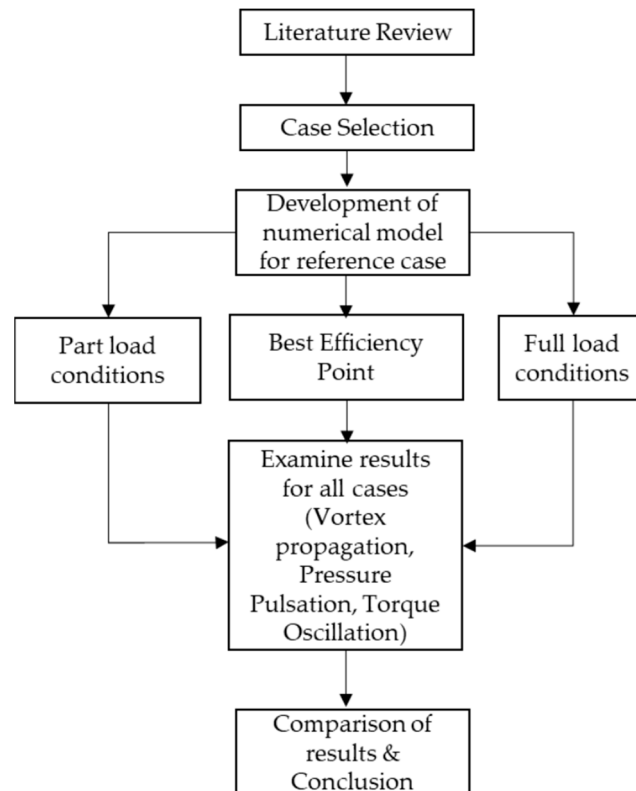

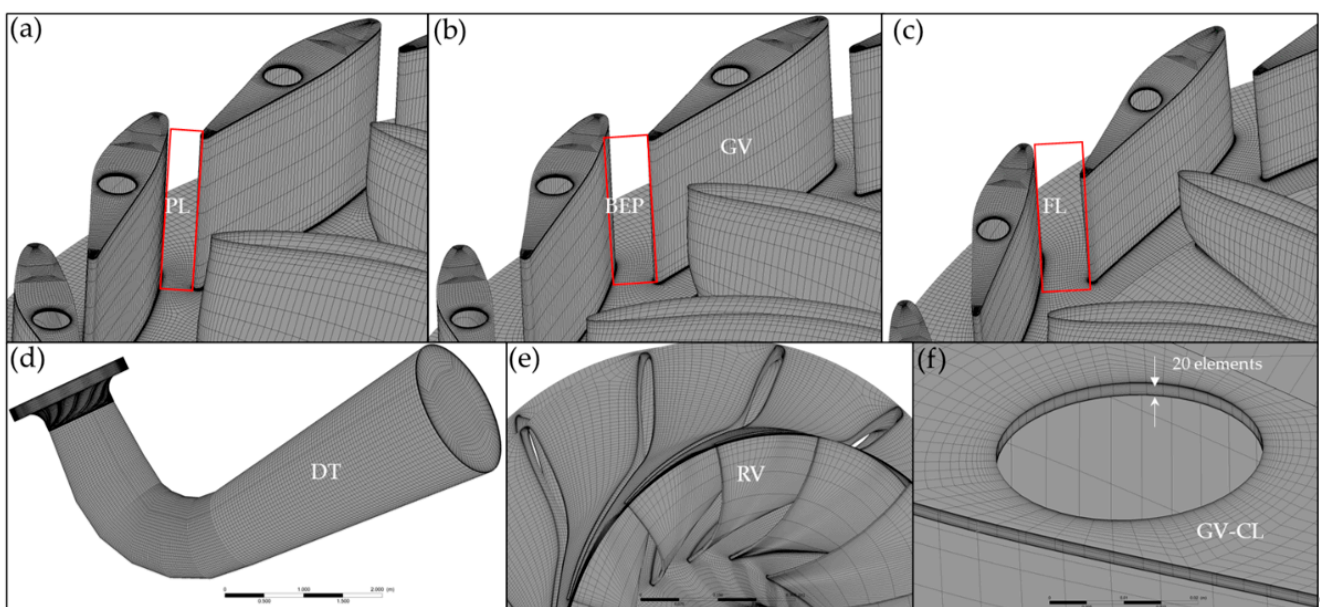**Figure 2.** Flow chart showing the methodology adopted in this work.

Figure 3. Structural grid for the runner, guide vanes with clearance gaps, and draft tube consisting of 7 million (approx.) elements. (**a**) GV at a partial load; (**b**) GV at the best efficiency point; (**c**) GV at a full load; (**d**) Draft tube; (**e**) Runner; (**f**) Clearance gap.

2.1. Mesh Generation and Boundary Conditions

Full passage modelling was carried out and the computational domain was discretized with a hexahedral structured mesh. ANSYS® Turbogrid™ was applied to generate the meshes in the runner and guide vanes, while the meshes in clearance gaps and draft tube were generated in ANSYS® ICEM CFD™. Meshes on the overall domain were well defined and the values of positive y-values were maintained below 30. A mass flow rate of 4330 kg/s at the circumferential inlet of guide vanes and average static pressure of 0 Pa at the outlet were chosen as boundary conditions for BEP case [24,25]. The designed mass flow rate of the turbine, representing 100% flow, was taken as the BEP. Interfaces between the stationary and rotational domain were considered with a frozen rotor method for steady-state analysis. This forms a local coupling which uses the rotating reference frame to save on computation by converting transient turbomachinery flow into a steady state. For transient analysis, a transient rotor–stator model was used as it accounts for all interaction effects between components that are in relative motion to each other and hence predicts the true transient interaction of the flow between a stator and rotor passage [26]. Transient simulations were carried out for total time corresponding to three runner revolutions, and at a time step of $1°$ of angular rotation for runners. The turbulence model selected for this study was the shear stress turbulence model developed by Meter [27], which was determined based upon the literature [28–30]. The details of the simulation settings are listed in Table 1.

Table 1. Numerical settings for the simulation.

Item	Setting
Inlet boundary condition	Mass flow rate at 4330 kg/s at BEP with a cylindrical flow component
Outlet boundary condition	Average static pressure of 0 Pa
Wall	No slip wall
Turbulence model	Shear stress transport
Turbulence intensity	Medium (5%)
Advection scheme	High resolution
Turbulence numeric	High resolution
Solver precision	Double
Convergence criteria	RMS residual below 1×10^{-5}

2.2. Mesh Sensitivity Analysis

The grid convergence index (GCI) method was used for the estimation of the discretization error and value extrapolation [31]. This particular technique has been found to be effective in predicting numerical uncertainties in the case of a Francis turbine [32,33]. For uncertainty analysis, three structured hexahedral meshes with different resolutions were created. Mesh refinement was performed by increasing the distribution in each direction. Uncertainties in the simulation were monitored by monitoring the torque and pressure inside the domain for three different points, i.e., VL1 (vaneless space), RV1 (runner blade) and DT1 (draft tube). The discretization error for the numerical model was determined as follows:

(i)　Average length of each element for a 3D mesh was determined as follows:

$$h = \left[\frac{1}{N} \sum_{i=1}^{N} (\Delta V_i) \right]^{1/3} \tag{1}$$

(ii)　Let $h_1 < h_2 < h_3$ and $r_{21} = h_2/h_1, r_{32} = h_3/h_2$. The apparent order was solved as in Equations (2)–(4) using a fixed point iteration method:

$$p = \frac{1}{\ln(r_{21})} |\ln|\varepsilon_{32}/\varepsilon_{21}| + q(p)| \tag{2}$$

$$q(p) = \ln\left(\frac{r_{21}^p - s}{r_{32}^p - s}\right). \tag{3}$$

$$s = 1.sign(\varepsilon_{32}/\varepsilon_{21}). \tag{4}$$

(iii)　The extrapolated values were calculated as follows:

$$\phi_{ext}^{21} = (r_{21}^p \phi_1 - \phi_2)/(r_{21}^p - 1) \tag{5}$$

(iv)　The approximate and extrapolated relative errors were calculated as follows:

$$e_a^{21} = \left|\frac{\phi_1 - \phi_2}{\phi_1}\right| \tag{6}$$

$$e_{ext}^{21} = \left|\frac{\phi_{ext}^{12} - \phi_1}{\phi_{ext}^{12}}\right| \tag{7}$$

$$GCI_{fine}^{21} = \frac{1.25 e_a^{21}}{r_{21}^p - 1} \tag{8}$$

Table 2 shows the uncertainties and extrapolated values. The numerical uncertainties in pressure at points 1 and 2, with a fine mesh and medium mesh, were 0.0151% and 0.2568%, respectively. Efficiency was calculated as the ratio of power output to input. Power output was calculated from the torque of the runner and its rotational speed, whereas power input was obtained from the net head. From the efficiency measurement, uncertainty for the fine mesh was 0.0307%.

Table 2. Discretization error for the reference case.

Parameter	Pressure 1 (Pa, Φ_1)	Pressure 2 (Pa, (Φ_2)	Efficiency (η, (Φ_3)
Coarse (G3)	366,912	344,516	90.15
Medium (G2)	367,151	344,112	91.84
Fine (G1)	367,236	345,083	92.03
ϕ_{ext}^{21}	367,280	345,791	92.05
e_a^{21}	0.02314%	0.0028%	0.0021%
GCI_{fine}^{21}	0.0151%	0.2568%	0.0307%

Figure 4a shows the normalized velocity at the outlet of the GV along the circumferential position at the trailing edge of GVs. Velocity in this case is normalized in terms of net head of the turbine as expressed in Equation (9).

$$v^*[-] = \frac{v}{\sqrt{2gH}} \tag{9}$$

where v = local velocity at the outlet of the GV, which is given as $v = \sqrt{v_x^2 + v_y^2}$.

For the numerical measurement of velocity, circumferential locations of the outlets of two GVs were considered such that the flow beneath the trailing edge of GV could be distinguished. A dimensionless term x/c was used in the x-axis, which denotes the position (x) from LE with respect to the chord length (c). In Figure 4, two different low velocity regions were observed due to the influence of the wake travelling from the trailing edge of the GV. Because of the influence of wakes and vortices travelling from the trailing edge, the uncertainties at these locations are higher, as shown in Figure 4b. As clearly observed in Figure 4a, the graph representing the coarse mesh has higher discrepancies as compared to the medium and fine meshes. Hence, the coarse mesh was discarded and the medium one was used for further numerical calculations.
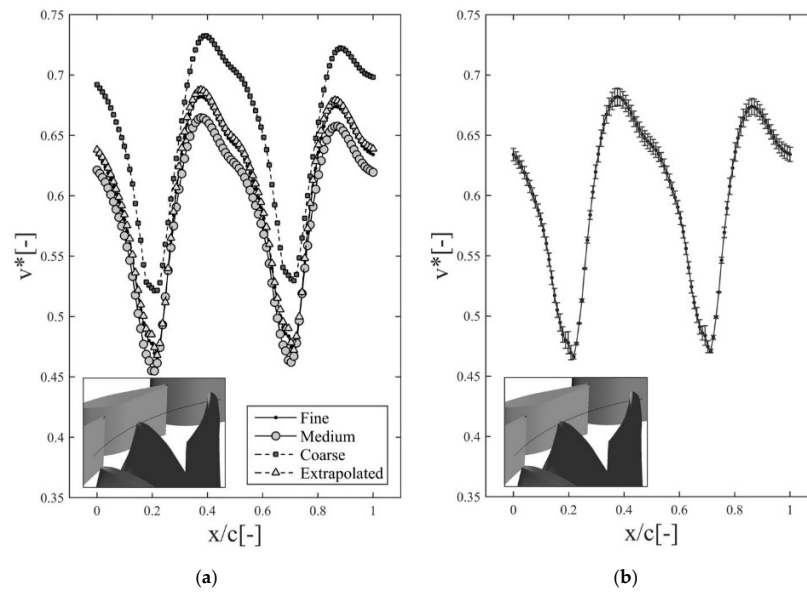
Figure 4. Uncertainty in velocity measurement at the outlet of the GV. (**a**) Different mesh schemes; (**b**) Discretization error bar.

2.3. Validation with Prototype Data

Steady-state simulations were conducted at designed and off-design conditions in the initial stage. Another set of simulations was carried out with the total pressure as the inlet boundary condition. The mass flow rate was calculated in a postprocessing step. Flow rate data available for the prototype turbine at different operating points [21] were compared with the results from the simulation as shown in Figure 5. It can be inferred from this figure that at the same guide vane opening angles, the resultant flow obtained from the CFD analysis closely matches the field data. Moreover, the efficiency comparison from the CFD calculation shows lower efficiency than the prototype measurement, which could be due to the overprediction of losses by the turbine with the use of the turbulence model [21]. It can be noticed at a deep partial load condition that the efficiency variation is higher than the designed point. In off-design conditions, the losses predicted by the numerical model are higher [7]. Figure 5 also shows the error bar which was constructed with the difference of numerical and experimental value for each GV opening angle.
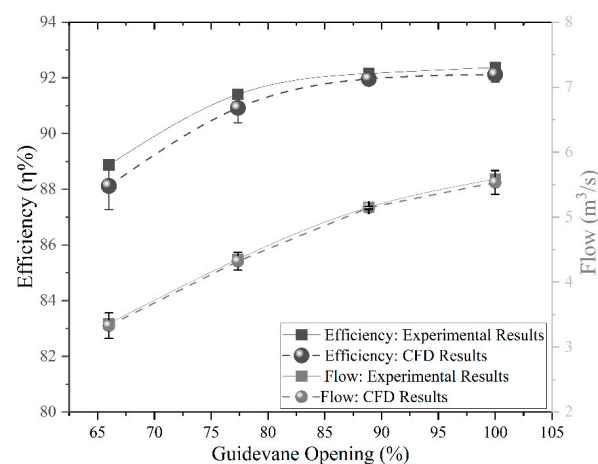

Figure 5. Prototype discharge and efficiency comparison with the simulated results for various operating condition.

Furthermore, validation of numerical model was also carried out by measuring the pressure around the middle GVs in three-GV cascade rigs developed by Chitrakar et al. [34].

The closed loop test setup was equipped with a pump delivering water from a lower reservoir. A flow meter was mounted at the outlet of the rig and two pressure taps were mounted at the inlet and outlet to acquire the correct operating points for measurement. The arrangement has a trapezoidal slot with holes with a diameter of 2 mm around the middle GV with a 2 mm offset from the GV surface. Piezoresistive pressure transducers were connected to these holes, which were used to determine GV loading. Figure 6 shows the experimental test section of the three-GV cascade rig that consists of a pressure measurement location at the middle GV (GV2). A pressure transducer was calibrated with a dead weight calibrator with an uncertainty of ±0.2%.

(**a**)   (**b**)

Figure 6. The three-GV test setup for experimental validation: (**a**) Experimental set up which shows the test section in the lab; (**b**) Locations of holes for tapping the value of pressure at GV.

Normalized pressure (Cp), which is the ratio of the pressure at a point to the pressure at an inlet as found by CFD analysis, was validated with the data obtained from the pressure transducer measurement around the circumferential positions from the leading edge to the trailing edge. Local pressure measurement at each measurement location was normalized by the pressure value at the leading edge of GV. Thus, the blade loading characterizing the flow around the GV was observed experimentally with a maximum normalized pressure where Cp = 1 at the leading edge [35]. In the CFD pressure measurement, at same experimental pressure measurement locations, pressure values were measured. It was seen that using the current numerical model, the maximum error in pressure measurement was 8.8% towards the leading edge in the pressure side of the GV. This might be due to the influence of GV1 and inappropriate stagnation as compared to the numerical solution. At all other locations of pressure measurement, the errors in the pressure measurement were less than 5%. The blade loading distribution of the current GV profile in the reference case is shown in Figure 7b.
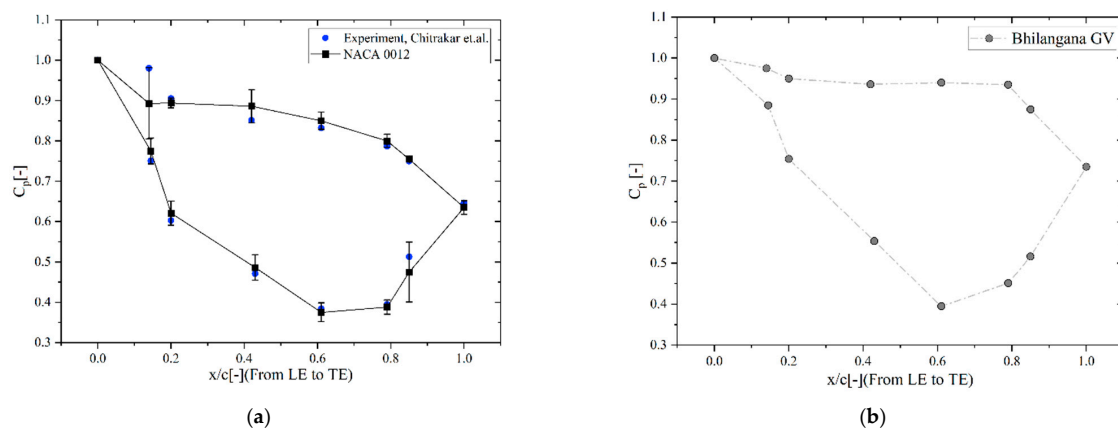

(**a**)   (**b**)

Figure 7. Validation of the CFD results with the experiment: (**a**) Velocity normal to camber line from LE to TE and pressure distribution in GV for NACA 0012 hydrofoil; (**b**) reference case GV profile.

3. Results and Discussions

3.1. Leakage Vortex from GV

Figure 8a shows the overall pattern of the GV leakage vortex obtained from the transient simulation for the BEP condition whereas Figure 8b shows three distinct leakage flow (LF) areas. Part 1 shows a LF initiating from the leading edge of GV, whereas part 2originates from the GV shaft region. From Figure 8b, it is clearly observed that LF from part 1 mixes with part 2 which ultimately strikes the leading edge of runner. Similarly, another LF is set up from the trailing edge of GV, which is further divided in part 3a and part 3b in Figure 8b. The intensity of these vortices can be related with the guide vane loading curve shown in Figure 7b. The pressure difference between the two sides of GV is maximum in the stream-wise location (x/c) of 0.5–0.7. As a result, the leakage flow is driven with higher acceleration, increasing the intensity of the vortex filament. Due to the difference in number of GVs and runner blades in the turbine, the region of vortices hitting the runner is different for each blade and in every revolution.
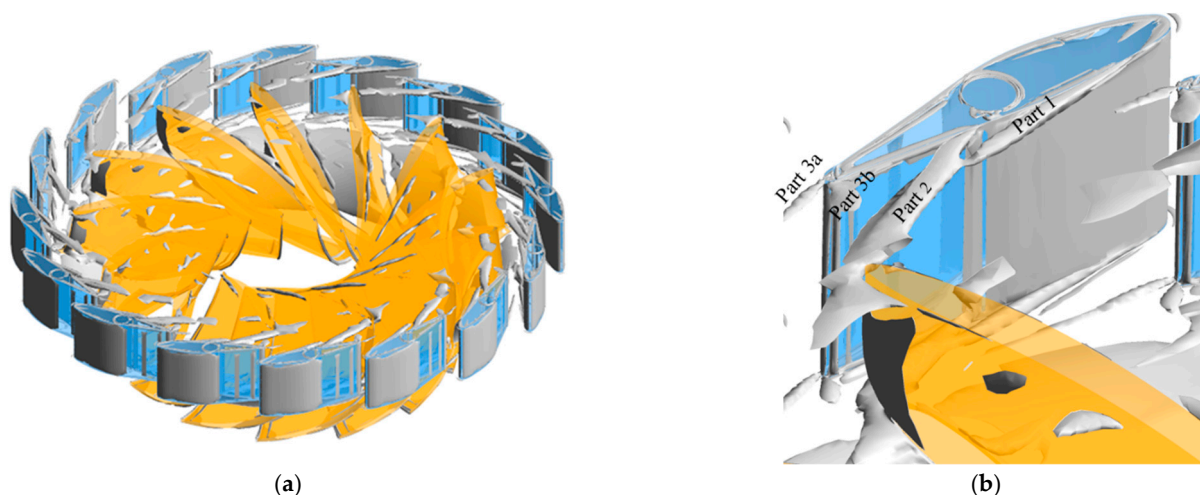

| (**a**) | (**b**) |

Figure 8. Leakage vortex from the GV: (**a**) Pattern as observed for complete set of GVs and runner blades; (**b**) Single GV and runner blade showing three distinct leakage flow areas.

3.2. Leakage Vortex Progression

Figure 9 shows the LV trajectory obtained by transient simulation. Among several vortex identification methods as discussed in the introduction part above, the Q criterion is considered for this work. It is usually suitable for vortex identification in incompressible fluid, especially in large scale vortex in turbulent flow [12]. The Q criterion identifies vortices using second invariant of velocity gradient tensor which is defined as follows:

$$Q = \frac{1}{2}tr(\nabla v)r^2 - tr\left(\nabla v^2\right) \tag{10}$$

where ∇v is the velocity gradient tensor and tr is the trace of the matrix.

A total of 13 points (P1 to P13) were located based on the vortex trajectory, as shown in Figure 9a, and vorticity was calculated on those points. Figure 9b shows the values of vorticity along LV trajectory for three operating conditions. Vorticity value was normalized in correspondence with BEP case, as shown in y axis of Figure 9b. Considering the propagation of LV from point P1, vorticity increases until point P2 for all cases and after point P3, it sharply drops until point P6. From point P6 to P9, it decreases slowly, and from P10 to P12, it is vorticity is almost lowest for the BEP and full load conditions as compared to the partial load condition from point P6 to P13 before striking the runner.
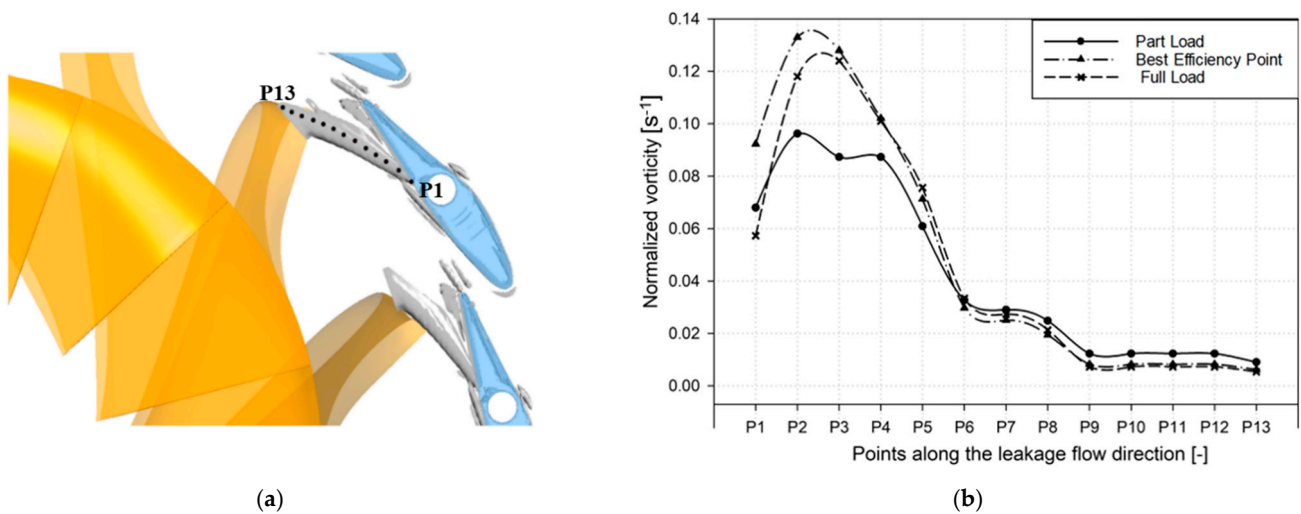
(a)

(b)

Figure 9. (**a**) LV pattern with 13 points along the trajectory for the calculation of vorticity value; (**b**) Vorticity graph normalized with corresponding BEP case along the LV trajectory.

Similarly, Figure 10 depicts values of turbulence kinetic energy (TKE) along the LV trajectory. The fluid undergoes irregular fluctuations or mixing during turbulent flow which can be visualized with irregular swirls of motions called eddies. Values of the TKE are directly related to the strength of turbulence in the flow. TKE, as seen in y-axis of Figure 10, was normalized with values corresponding to the BEP. TKE increased from points P1 to P3 steadily and then produced a sharp increase until point P5, i.e., almost approaching the middle of the trajectory. The value of TKE from point P5 fell rapidly until P9, where it then stabilized until the end of propagation. The TKE strength was lowest for the BEP and full load conditions in comparison with partial load condition after point 6 as the LV reached the leading edge of runner, which is a similar pattern to that observed for the vorticity graph shown in Figure 9b.
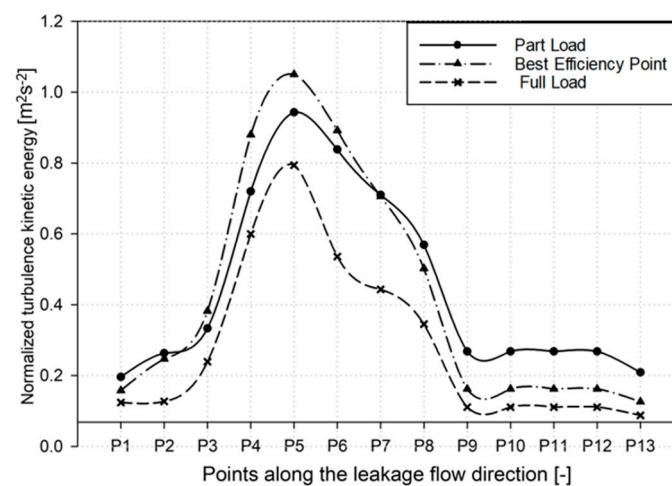

Figure 10. Turbulence kinetic energy variation along the LV trajectory.

Transient simulations were performed for three operating conditions to inspect spatial-temporal progression of LV before it hits the leading edge of runner blades. Figure 11a–f show the evolution of the LV as one runner blade passes from one GV to the consecutive GV. It shows the vortex for a 10° revolution, capturing 2° at a time. For the investigation of the progression of the part II LV of the hub region, which strikes the leading edge of runner, it can be categorized into three stages, namely (a) the elongation stage, (b) disintegration stage, and (c) dissolving stage. The elongation stage represents some shedding and the LV

being slender and weaker as seen in Figure 11b,c. Figure 11d,e shows the disintegration stage, in which LV becomes more stretched with a decrease in volume and length. Only a few traces of the LV can be observed in Figure 11f, which can be described as the dissolving stage. The same process is expected to continue as the runner rotates. The LV at the shroud region is shown by the green ellipse in Figure 11a and is transported all the way until the mid-section of the blade before the majority of the vortex is dissolved.
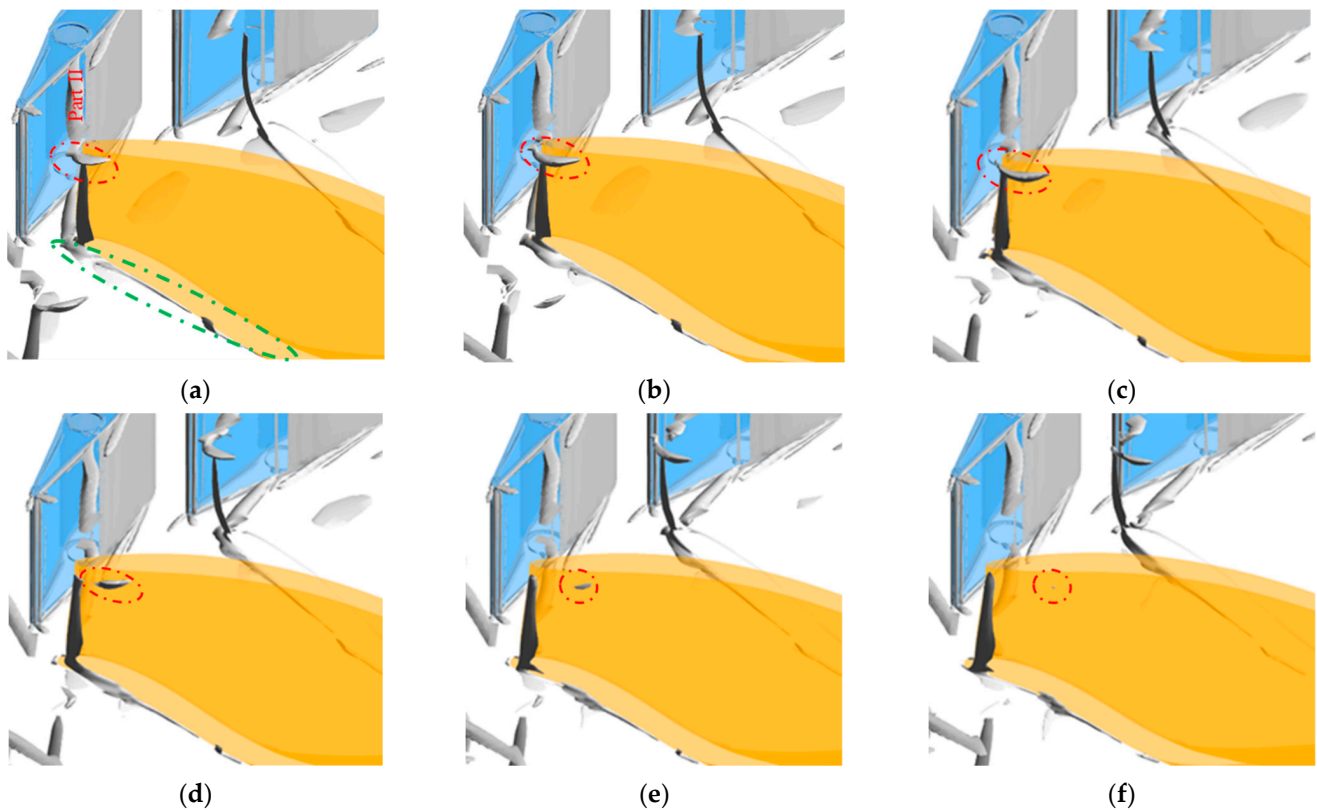

Figure 11. Progression of leakage vortex during runner rotation at BEP: (**a**) T_0; (**b**) $T_0 + 1/5$ of $X°$; (**c**) $T_0 + 2/5$ of $X°$; (**d**) $T_0 + 3/5$ of $X°$; (**e**) $T_0 + 4/5$ of $X°$; (**f**) $T_0 + X°$.

Figure 12a–f show the propagation of LV during $10°$ of rotation of the runner during the partial load condition. It also follows the same trend as in case of BEP, but the vortex disintegrates and dissolves earlier than BEP. For this condition, vortex almost disappear in Figure 12e but while compared to the same position for BEP, there is still some traces of vortex during that time. In partial load conditions, the pressure difference between the two sides of the GVs rises (because of the closing), so logically the intensity of the vortex should also rise. In this case, we saw that the intensity dropped instead, and this may be due to the reduced flow rates in the part load condition.

Similarly, the progression of the leakage vortex for full load conditions is depicted in Figure 13a–f. In this case, the strength and volume of LF at the hub and shroud is higher than in previous cases. Some amount of a vortex still exists before another set of LF from consecutive GV hits the runner blade. At full load conditions, due to opening, the pressure difference should be minimum; however, in this case, the flow rate is high, and this could be the reason why we see high intensity vortices compared to other cases.

The formation of complex vortices can represent significant influences on the performance and flow stability of hydraulic machinery. Insertion of points in the trajectory which corresponds to LV progression helped to compute the value of vorticity and TKE which are the vital parameters with major influence on the flow pattern. Intensity of these vortices can be related to GV loading curve. Similarly, the strength of turbulence in the flow can be related to the value of the TKE.
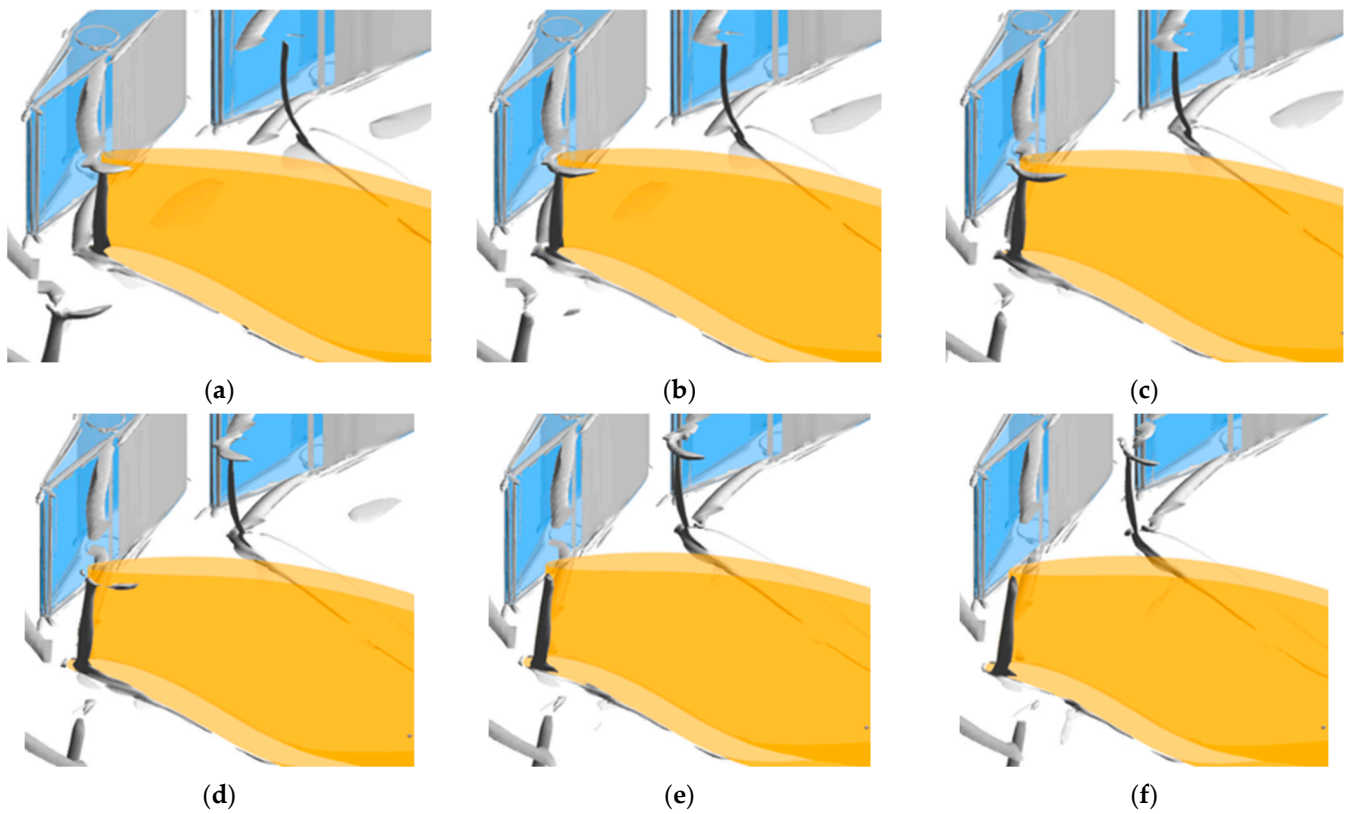
Figure 12. Progression of leakage vortex during runner rotation at part load: (**a**) T_0; (**b**) $T_0 + 1/5$ of $X°$; (**c**) $T_0 + 2/5$ of $X°$; (**d**) $T_0 + 3/5$ of $X°$; (**e**) $T_0 + 4/5$ of $X°$; (**f**) $T_0 + X°$.
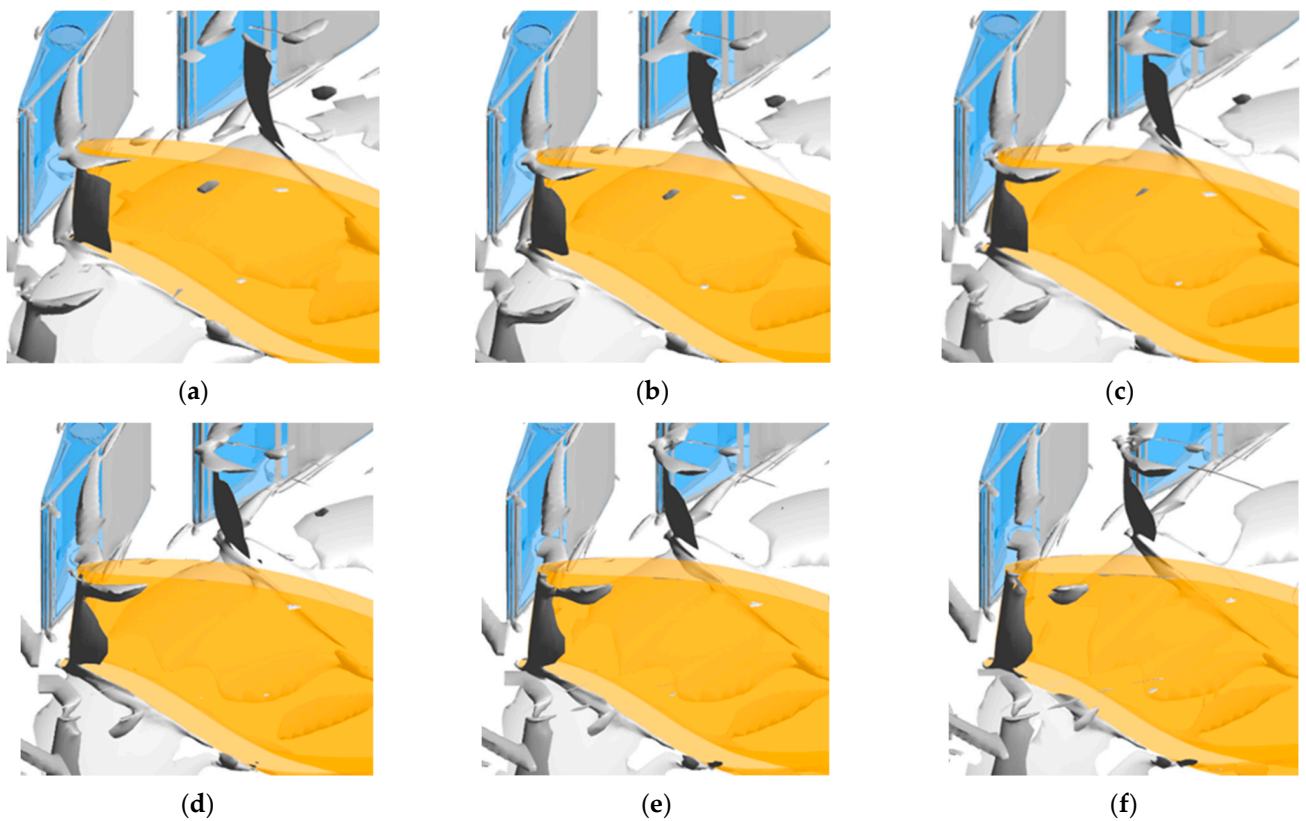
Figure 13. Progression of leakage vortex during runner rotation at full load: (**a**) T_0; (**b**) $T_0 + 1/5$ of $X°$; (**c**) $T_0 + 2/5$ of $X°$; (**d**) $T_0 + 3/5$ of $X°$; (**e**) $T_0 + 4/5$ of $X°$; (**f**) $T_0 + X°$.

3.3. Pressure Pulsations Inside Runner

The stationary domain experiences pressure fluctuations at a frequency corresponding to the number of rotating blades (z_b) and the rotational speed of the runner (n), as shown in Equation (11). Likewise, rotating domain experience a frequency (f_{gv}) corresponding to number of guide vanes (z_{gv}) and rotational speed of runner (n), as shown in Equation (12) [33,36,37].

$$f_b = n \cdot z_b \quad [\text{Hz}] \tag{11}$$

$$f_{gv} = n \cdot z_{gv} \ [\text{Hz}] \tag{12}$$

A total of sixteen points were located in the vaneless space, runner blade and draft tube, as shown in Figure 14a,b, to analyze frequency spectra. Among the sixteen points, six points from DT1 to DT6 were located in the draft tube passage from the runner outlet to the draft tube outlet. Similarly, four points, from VL1 to VL4, starting from hub area to shroud area, were defined in the vaneless space before the leading edge of runner. The remaining six points, namely, RV1 to RV6, starting from leading edge to trailing edge of the blade, were inserted along the runner blade. Pressure pulsation was calculated by subtracting the mean pressure (p) from the instantaneous pressure ($\overline{p}$) and was normalized by the reference pressure ($\rho E)_{BEP}$ [38].

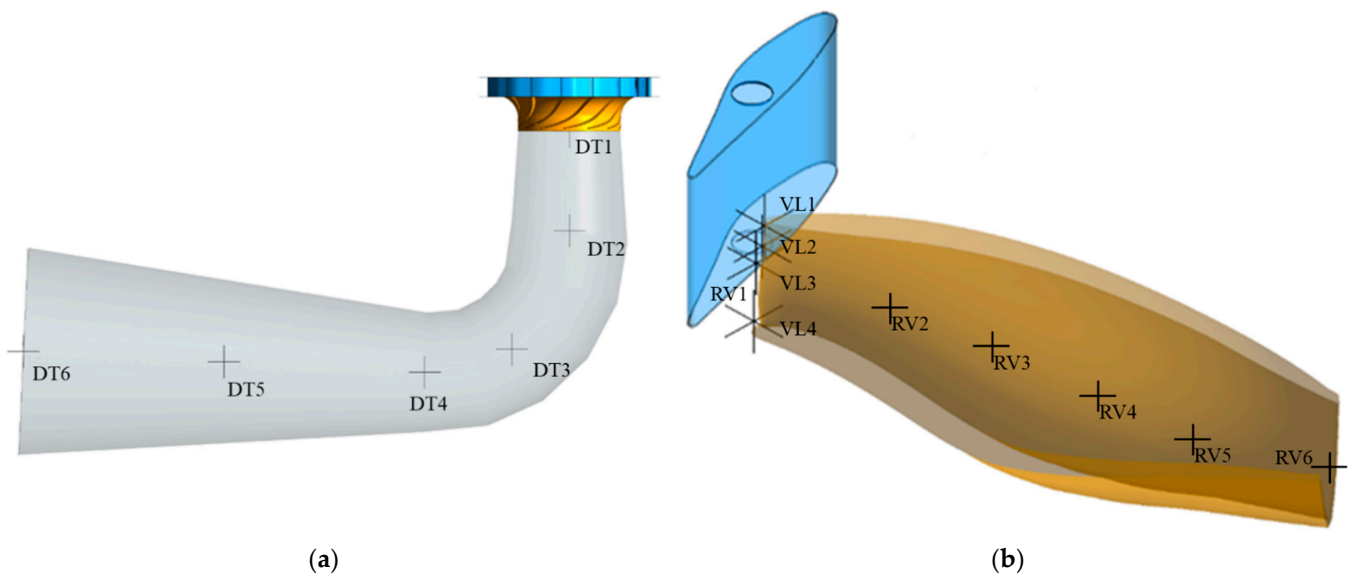$$p* = \frac{p - \overline{p}}{(\rho E)_{BEP}} \quad [-] \tag{13}$$

Figure 14. Points for measurement of pressure pulsations at: (**a**) Six points from DT1 to DT6 inside the draft tube domain; (**b**) Four points from VL1 to VL4 inside the vaneless space and six points from RV1 to RV6 in the runner blade surface for pressure monitoring.

In a high-head Francis turbine, as in the reference case of this study, the vaneless space between the guide vane and runner blade is small. Pressure fluctuations associated to RSI are a major concern in such an area, as several failures related to hydraulic turbines are related to this phenomenon [39]. Figure 15 shows the Fourier-transformed pressure pulsation for three operating conditions at vaneless space with a sampling frequency of 4500 Hz. The research case presented here is comprised of 16 guide vane blades. For the runner rotation of 750 rpm, the value of f_{gv} for the runner is 200 Hz. The first peak observed in Figure 15 represents the guide vane passing frequency. Consequently, other successive harmonics occurs at $2f_b = 400$ Hz, $3f_b = 600$ Hz, and so on. The pulsating signal is seen in

every point for each operating conditions. It shows that pressure pulsating amplitude is most significant while operating the runner in part load conditions.
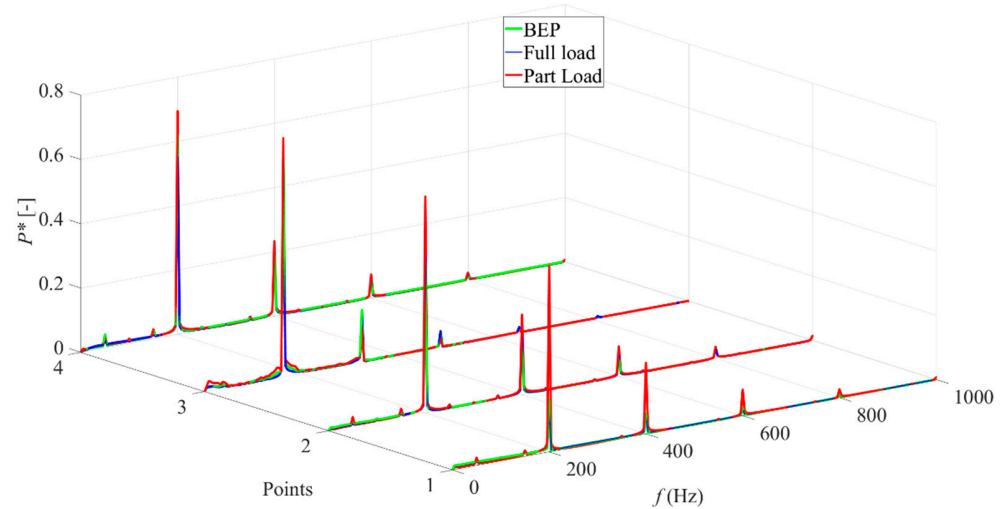

Figure 15. Frequency spectrum of pressure time signals at vaneless space.

Figure 16 shows FFT analysis of pressure pulsation inside the draft tube. As demonstrated in the figure, peak pressure pulsation is at 4 Hz for all measured points which is 0.32 times that of runner rotational frequency. After that other pulsations occur at 8 Hz, 12 Hz, 16 Hz which corresponds to 0.64, 0.96, and 1.28 times the runner rotational frequency, respectively. This phenomenon can be related with the hydroacoustic pressure waves investigation by Arpe et al. [40], where about two types of pressure fluctuations related to vortex precession (a) in the range of 0.3–0.4 f_n, and (b) in the range of 2–4 f_n, as pointed out during the experiment.
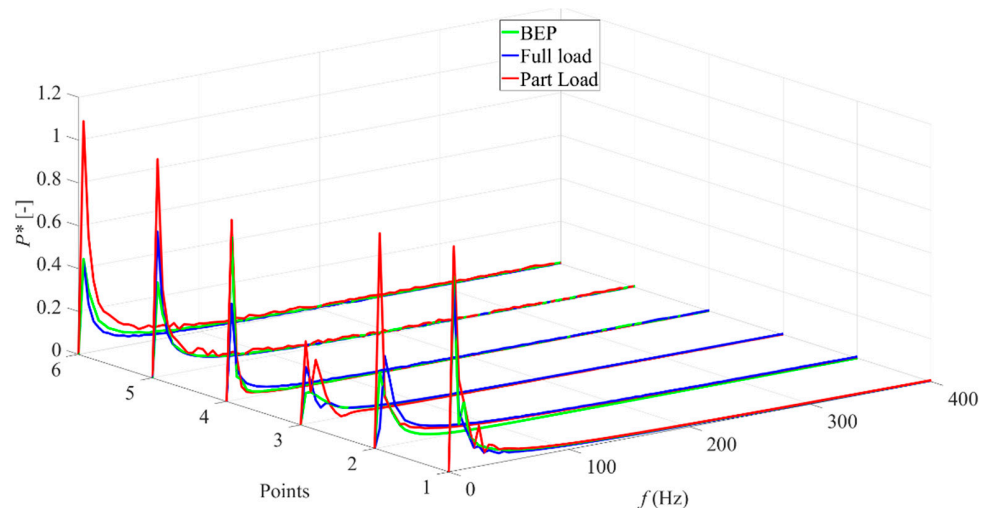

Figure 16. Frequency spectrum of pressure time signals inside draft tube.

FFT plot of pressure fluctuation from points RV1 to RV6 along the runner blade is presented in Figure 17. It is assumed that the points located in the runner surface rotate with the runner, hence the value obtained is during runner operation. It is evident from the figure that the periodic behavior of pressure fluctuation is governed by both frequencies. The low frequencies of 0.32, 0.64, and 0.96 times the runner rotational frequency correspond to the rotating vortex rope (RVR) frequency and its harmonics [41]. The bigger frequencies of 200 Hz, 400 Hz, and 600 Hz correspond to the guide vane passing frequency and its harmonics.
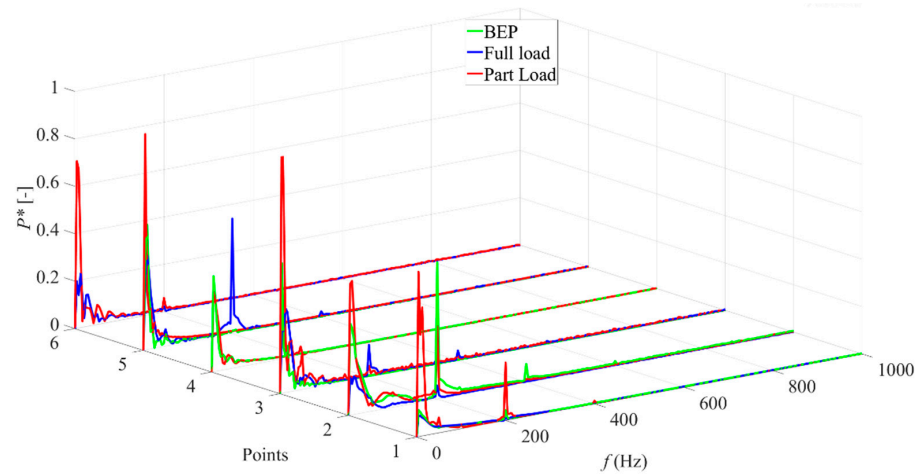
Figure 17. Frequency spectrum of pressure time signals along runner blade.

Frequency spectrum of pressure time signals showed that operation outside the BEP can result in high amplitudes and vortex roping, which can cause serious damage to the runner and other components. A swirling component will occur in the draft tube outside BEP operation. The high velocities in vortex core can decrease the pressure, resulting in a vapor-filled cavity core. This can cause operational challenges when coinciding with dynamics oscillations in a system.

3.4. Torque Oscillations

RSI between guide vanes and runner induces pressure fluctuations inside the runner, which causes torque fluctuation. Fluctuation in torque inside the runner is caused by the expanding wakes from the guide vanes, which progresses until runner blades [42]. Hydraulic torque (T_h) from the water acts on the runner, thus accelerating it. T_h is a function of hydraulic power (P_h) and angular velocity (ω), as expressed in Equation (14). Figure 18 shows the dynamic forces in runner blade showing an average torque for three operating conditions plotted against runner angular position.

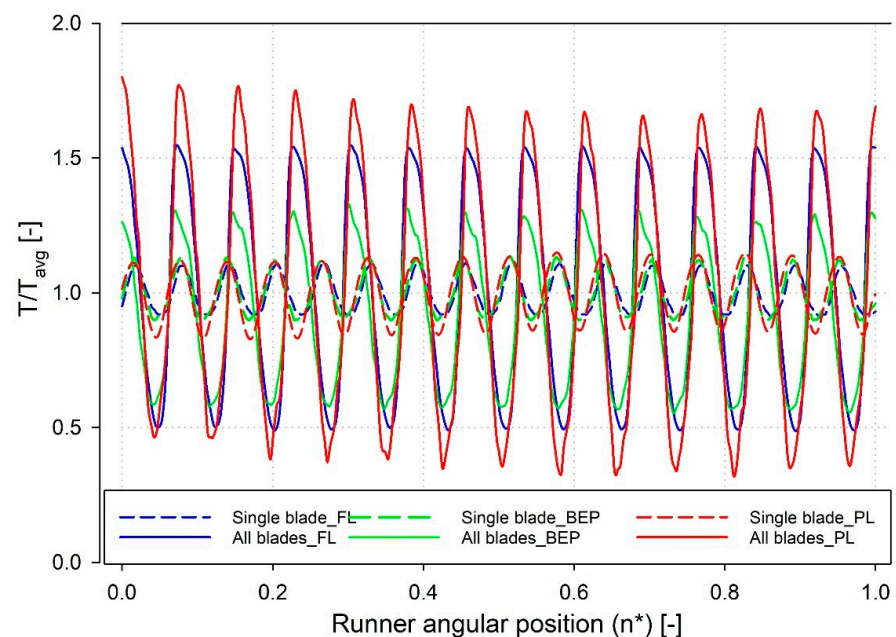$$T_h = \frac{P_h}{\omega} \; [\text{Nm}] \tag{14}$$

Figure 18. Torque oscillations for various operating conditions.

Torque is normalized with the value corresponding for the BEP conditions. The patterns of torque fluctuations across different operating conditions are quite similar but the amplitude varies for all. The highest fluctuation of torque is observed at part load condition of operating stage shown by red graph in Figure 18, which is followed by the full load condition shown by the blue graph. The lowest torque fluctuation of all can be seen in BEP condition as shown by the green graph. The larger fluctuations were obtained for the full runner as compared to single blade for all cases, which agrees with the work done by Nicolle et al. [43]. For the single blade, a total of 16 peaks can be seen which is due to RSI arising from pressure fields around the guide vane and it corresponds to guide vanes number; however, for the full runner, 13 peaks are seen for all cases. The reason behind this is that the number of runner blades is a prime number and has no common integer with the number of guide vanes. As such, the torque variation for the runner must be completed in one pitch, i.e., 360/13. This phenomenon can also be explained with the assumption that when we consider full runner, more than one blade is experiencing RSI at the same time.

4. Conclusions

This work features an exploration of the spatial temporal progression of a leakage vortex in a high-head Francis turbine. The LV evolution and trajectory, LV progression from the clearance gap to runner blades, vortex dynamics, and pressure fluctuations have been analyzed in this study based on numerical simulations.

LV pattern and trajectory data were acquired from transient simulations. Vortex core intensity in the leakage flow decreased along the progression. The progression of leakage flow at the hub area was classified into three forms, i.e., the elongation stage, disintegration stage, and dissolving stage. Leakage flow at the shroud area is transported until the mid-section of the blade, i.e., before the majority of vortex is dissolved, and seems to pass from the outlet of the runner as well. The values of vorticity and TKE along the LV trajectory somehow gave a clear picture of the complex vortices and turbulence phenomena for varying operating cases.

Unsteady pressure fluctuations were investigated with the reference turbine at three operating conditions, i.e., BEP, partial loading, and full loading. A total of sixteen points were located in the vaneless space, runner blade, and draft tube to study the pressure pulsations in the stationary and rotating domains. The frequency spectra data of pressure signals in the vaneless space showed the highest amplitude at the guide vane passing frequency (*fgv*) and its successive harmonics, i.e., 2*fgv*, 3*fgv*, 4*fgv* and so on, due to RSI. Monitoring the points at the draft tube showed peak pressure pulsation that was 0.32 times that of the runner rotational frequency and subsequent peaks for its harmonics. The points located along the runner blade from the leading edge to the trailing edge showed that the frequency spectrum was affected by both available frequencies. Low frequencies of 0.32, 0.64, and 0.96 times the runner rotational frequency corresponded to the rotating vortex rope frequency and its harmonics, whereas higher frequencies of 200 Hz, 400 Hz, and 600 Hz corresponded to the guide vane passing frequency and its harmonics. Moreover, while taking torque fluctuations for different operating conditions into account, it was observed that the patterns were quite similar in terms of the variation of amplitude. The highest fluctuation of the torque was observed at partial load condition, followed by the full load condition, and least for the BEP condition.

In summary, important dynamic characteristics for leakage vortex evolution and progression have been revealed in this work. The frequency spectra of pressure signals at various locations in the turbine provide some information regarding pressure fields in the blade channel; however, the spatial temporal evolution of a vortex is complex phenomenon which is governed by several factors. Further investigation is needed for overall energy improvement and the elucidation of a novel technique for vortex suppression before hitting a runner. Grooves or shapes can be added and studied which could reduce the flow separation and pressure gradient between two sides of the CG and hence suppress the

LV along the way. This method should be extensively developed for implementation in real scenarios.

Nomenclature

GCI_{fine}	Grid convergence index of the fine mesh [-]
e_a	Approximate relative error [-]
e_{ext}	Extrapolated relative error [-]
f_b	Blade passing Frequency [Hz]
f	Frequency [Hz]
H	Head [m]
n	Rotation of the runner [rpm]
P_h	Power [kW]
P^*	Normalized Pressure [-]
T_h	Hydraulic torque [Nm]
T_{avg}	Average torque [Nm]
ω	Angular velocity [rads^{-1}]
Φ	Variable for GCI calculation [-]
v^*	Normalized velocity [-]
v	Local velocity [ms^{-1}]
Cp	Normalized pressure [-]
ρ	Density [kgm^{-3}]
E	Specific hydraulic energy of turbine [J kg^{-1}]
Z_b	Number of rotating blades [-]
Z_{gv}	Number of guide vanes [-]

References

1. Brekke, H. The influence from the Guide Vane Clearance Gap on Efficiency and Scale Effect for Francis Turbine. In Proceedings of the IAHR Symposium on Progress within Large and High Specific Energy Units, Trondheim, Norway, 20–23 June 1988; Volume 14, pp. 825–837.
2. Thapa, B.S.; Dahlhaug, O.G.; Thapa, B. Sediment Erosion Induced Leakage Flow from Guide Vane Clearance Gap in a Low Specific Speed Francis Turbine. *Renew. Energy* **2017**, *107*, 253–261. [CrossRef]
3. Chitrakar, S.; Thapa, B.S.; Dahlhaug, O.G.; Neopane, H.P. Numerical Investigation of the Flow Phenomena around a Low Specific Speed Francis Turbine's Guide Vane Cascade. *IOP Conf. Ser. Earth Environ. Sci.* **2016**, *49*. [CrossRef]
4. Koirala, R.; Thapa, B.; Neopane, H.P.; Zhu, B.; Chhetry, B. Sediment Erosion in Guide Vanes of Francis Turbine: A Case Study of Kaligandaki Hydropower Plant, Nepal. *Wear* **2016**, *362–363*, 53–60. [CrossRef]
5. Koirala, R.; Zhu, B.; Neopane, H.P. Effect of Guide Vane Clearance Gap on Francis Turbine Performance. *Energies* **2016**, *9*, 275. [CrossRef]
6. Liu, Y.; Han, Y.; Tan, L.; Wang, Y. Blade Rotation Angle on Energy Performance and Tip Leakage Vortex in a Mixed Flow Pump as Turbine at Pump Mode. *Energy* **2020**, *206*, 118084. [CrossRef]
7. Chitrakar, S.; Dahlhaug, O.G.; Neopane, H.P. Numerical Investigation of the Effect of Leakage Flow through Erosion-Induced Clearance Gaps of Guide Vanes on the Performance of Francis Turbines. *Eng. Appl. Comput. Fluid Mech.* **2018**, *12*, 662–678. [CrossRef]
8. Chitrakar, S.; Neopane, H.P.; Dahlhaug, O.G. Particle Image Velocimetry Investigation of the Leakage Flow through Clearance Gaps in Cambered Hydrofoils. *J. Fluids Eng. Trans. ASME* **2017**, *139*. [CrossRef]

9. Gautam, S.; Neopane, H.P.; Thapa, B.S.; Chitrakar, S.; Zhu, B. Numerical Investigation of the Effects of Leakage Flow from Guide Vanes of Francis Turbines Using Alternative Clearance Gap Method. *J. Appl. Fluid Mech.* **2020**, *13*, 1407–1419. [CrossRef]
10. Liu, Y.; Tan, L.; Wang, B. A Review of Tip Clearance in Propeller, Pump and Turbine. *Energies* **2018**, *11*, 2202. [CrossRef]
11. Kobro, E. Measurement of Pressure Pulsations in Francis Turbines. Ph.D. Thesis, NTNU, Trondheim, Norway, 2010.
12. Zhang, Y.; Liu, K.; Xian, H.; Du, X. A Review of Methods for Vortex Identification in Hydroturbines. *Renew. Sustain. Energy Rev.* **2018**, *81*, 1269–1285. [CrossRef]
13. Qian, R. Flow Field Measurements in a Stator of a Hydraulic turbine. Ph.D. Thesis, Laval University, Quebec, QC, Canada, 2008.
14. Chakraborty, P.; Balachandar, S.; Adrian, R.J. On the Relationships between Local Vortex Identification Schemes. *J. Fluid Mech.* **2005**, *535*, 189–214. [CrossRef]
15. Elsas, J.H.; Moriconi, L. Vortex Identification from Local Properties of the Vorticity Field. *Phys. Fluids* **2017**, *29*. [CrossRef]
16. ANSYS Inc. ANSYS Inc. ANSYS CFD-Post User's Guide. In *Vortex Core Region*; ANSYS Inc: Canonsburg, PA, USA, 2017.
17. Hunt, J.C.R.; Wray, A.A.; Eddies, P.M. Streams, and Convergence Zones in Turbulent Flows. In *Center for Turbulence Research, Proceedings of the Summer Program*; Stanford University: Stanford, CA, USA, 1988; pp. 193–208.
18. Jeong, J.; Hussain, F. On the Identification of a Vortex. *J. Fluid Mech.* **1995**, 69–94. [CrossRef]
19. Chong, M.S.; Perry, A.E.; Cantwell, B.J. A General Classification of Three-Dimensional Flow Fields. *Phys. Fluids A* **1990**, *2*, 765–777. [CrossRef]
20. Zhou, J.; Adrian, R.J.; Balachandar, S.; Kendall, T.M. Mechanisms for Generating Coherent Packets of Hairpin Vortices in Channel Flow. *J. Fluid Mech.* **1999**, *387*, 353–396. [CrossRef]
21. Thapa, R.; Sharma, S.; Singh, K.M.; Gandhi, B.K. Numerical Investigation of Flow Field and Performance of the Francis Turbine of Bhilangana-III Hydropower Plant. *J. Phys. Conf. Ser.* **2020**, *1608*. [CrossRef]
22. Acharya, N.; Trivedi, C.; Wahl, N.M.; Gautam, S.; Chitrakar, S.; Dahlhaug, O.G. Numerical Study of Sediment Erosion in Guide Vanes of a High Head Francis Turbine. *J. Phys. Conf. Ser.* **2019**, *1266*. [CrossRef]
23. Gautam, S.; Neopane, H.P.; Acharya, N.; Chitrakar, S.; Thapa, B.S.; Zhu, B. Sediment Erosion in Low Specific Speed Francis Turbines: A Case Study on Effects and Causes. *Wear* **2020**, *442–443*. [CrossRef]
24. *IEC 60041: 1991–11; Field Acceptance Tests to Determine the Hydraulic Performance of Hydraulic Turbines, Storage Pumps and Pump-Turbines*; International Electrotechnical Commission: Geneva, Switzerland, 1991.
25. Trivedi, C.; Dahlhaug, O.G. A Comprehensive Review of Verification and Validation Techniques Applied to Hydraulic Turbines. *Int. J. Fluid Mach. Syst.* **2019**, *12*, 345–367. [CrossRef]
26. Ansys Inc. CFX Solver Modelling Guide, Release 15.0. *ANSYS CFX Solver Model. Guid.* **2013**, *15317*, 724–746.
27. Menter, F.R. Review of the Shear-Stress Transport Turbulence Model Experience from an Industrial Perspective. *Int. J. Comut. Fluid Dyn.* **2009**, *23*, 305–316. [CrossRef]
28. Gautam, S.; Lama, R.; Chitrakar, S.; Thapa, B.S.; Zhu, B.; Neopane, H.P. Numerical Investigation on the Effects of Leakage Flow from Guide Vane-Clearance Gaps in Low Specific Speed Francis Turbines. *J. Phys. Conf. Ser.* **2020**, *1608*. [CrossRef]
29. Trivedi, C.; Cervantes, M.J.; Dahlhaug, O.G. Numerical Techniques Applied to Hydraulic Turbines: A Perspective Review. *Appl. Mech. Rev.* **2016**, *68*, 1–18. [CrossRef]
30. Arispe, T.M.; de Oliveira, W.; Ramirez, R.G. Francis Turbine Draft Tube Parameterization and Analysis of Performance Characteristics Using CFD Techniques. *Renew. Energy* **2018**, *127*, 114–124. [CrossRef]
31. Celik, I.B.; Ghia, U.; Roache, P.J.; Freitas, C.J.; Coleman, H.; Raad, P.E. Procedure for Estimation and Reporting of Uncertainty Due to Discretization in CFD Applications. *J. Fluids Eng. Trans. ASME* **2008**, *130*, 0780011–0780014. [CrossRef]
32. Trivedi, C.; Cervantes, M.J.; Gandhi, B.K.; Dahlhaug, O.G. Experimental and Numerical Studies for a High Head Francis Turbine at Several Operating Points. *J. Fluids Eng. Trans. ASME* **2013**, *135*, 1–17. [CrossRef]
33. Shingai, K.; Okamoto, N.; Tamura, Y.; Tani, K. Long-Period Pressure Pulsation Estimated in Numerical Simulations for Excessive Flow Rate Condition of Francis Turbine. *J. Fluids Eng. Trans. ASME* **2014**, *136*, 1–9. [CrossRef]
34. Chitrakar, S.; Neopane, H.P.; Dahlhaug, O.G. Development of a Test Rig for Investigating the Flow Field around Guide Vanes of Francis Turbines. *Flow Meas. Instrum.* **2019**, *70*, 101648. [CrossRef]
35. Chitrakar, S.; Thapa, B.S.; Dahlhaug, O.G.; Neopane, H.P. Numerical and Experimental Study of the Leakage Flow in Guide Vanes with Different Hydrofoils. *J. Comput. Des. Eng.* **2017**, *4*, 218–230. [CrossRef]
36. Trivedi, C.; Agnalt, E.; Dahlhaug, O.G.; Brandastro, B.A. Signature Analysis of Characteristic Frequencies in a Francis Turbine. *IOP Conf. Ser. Earth Environ. Sci.* **2019**, *240*. [CrossRef]
37. Laouari, A.; Ghenaiet, A. Predicting Unsteady Behavior of a Small Francis Turbine at Several Operating Points. *Renew. Energy* **2019**, *133*, 712–724. [CrossRef]
38. Trivedi, C.; Cervantes, M.J.; Gandhi, B.K. Investigation of a High Head Francis Turbine at Runaway Operating Conditions. *Energies* **2016**, *9*, 149. [CrossRef]
39. Dorji, U.; Ghomashchi, R. Hydro Turbine Failure Mechanisms: An Overview. *Eng. Fail. Anal.* **2014**, *44*, 136–147. [CrossRef]
40. Arpe, J.; Nicolet, C.; Avellan, F. Experimental Evidence of Hydroacoustic Pressure Waves in a Francis Turbine Elbow Draft Tube for Low Discharge Conditions. *J. Fluids Eng. Trans. ASME* **2009**, *131*, 0811021–0811029. [CrossRef]
41. Zhou, X.; Shi, C.; Miyagawa, K.; Wu, H.; Yu, J.; Ma, Z. Investigation of Pressure Fluctuation and Pulsating Hydraulic Axial Thrust in Francis Turbines. *Energies* **2020**, *13*, 1734. [CrossRef]

42. Anup, K.C.; Thapa, B.; Lee, Y.H. Transient Numerical Analysis of Rotor-Stator Interaction in a Francis Turbine. *Renew. Energy* **2014**, *65*, 227–235. [CrossRef]
43. Nicolle, J.; Cupillard, S. Prediction of Dynamic Blade Loading of the Francis-99 Turbine. *J. Phys. Conf. Ser.* **2015**, *579*. [CrossRef]